

Proposal for a Damping-Ring-Free Electron Injector for Future Linear Colliders

T. Xu,^{1,*} M. Kuriki,² P. Piot,^{1,3} and J. G. Power³

¹*Northern Illinois Center for Accelerator & Detector Development and Department of Physics,
Northern Illinois University, DeKalb, IL 60115, USA*

²*Hiroshima University, Higashi-hiroshima, Hiroshima, Japan 739-8527*

³*Argonne National Laboratory, Lemont, IL 60439, USA*

(Dated: May 10, 2022)

The current designs of future electron-positron linear colliders incorporate large and complex damping rings to produce asymmetric beams for beamstrahlung suppression. Here we present the design of an electron injector capable of delivering flat electron beams with phase-space partition comparable to the electron-beam parameters produced downstream of the damping ring in the proposed international linear collider (ILC) design. Our design does not employ a damping ring but is instead based on cross-plane phase-space-manipulation techniques. The performance of the proposed configuration, its sensitivity to jitter along with its impact on spin-polarization is investigated. The proposed paradigm could be adapted to other linear collider concepts under consideration and offers a path toward significant cost and complexity reduction.

PACS numbers: 29.27.a, 41.75.Fr, 41.85.p

I. INTRODUCTION

High-energy electron-positron (e^-/e^+) collisions have been invaluable engine of discovery in elementary-particle physics. TeV-class linear colliders (LC) will give access to energy-scale beyond the Standard Model [1]. A critical metric to quantify the performances of an LC is the luminosity defined as

$$\mathfrak{L} = \frac{P_b}{E_b} \left(\frac{N}{4\pi\sigma_x^*\sigma_y^*} \right), \quad (1)$$

where N the single-bunch population, E_b and P_b respectively the energy and power associated with the beams and σ_i^* refers to the horizontal ($i = x$) and vertical ($i = y$) beam sizes at the interaction point. During collision beam-beam interaction results in an envelop pinch which enhances luminosity while also resulting in an increase in energy spread due to beamstrahlung effects [2]. A technique to mitigate beamstrahlung consists in using flat beams $\sigma_y \ll \sigma_x$ [3]. In such a configuration the luminosity takes the form

$$\mathfrak{L} = \frac{P_b}{E_b} \frac{\sqrt{5}}{16\alpha^2\sqrt{3}r_e\pi} \frac{\sqrt{\gamma n_\gamma^3}}{\sqrt{\sigma_z}\sigma_y^*} \quad (2)$$

where r_e is the classical radius of an electron, $\alpha \simeq 1/137$ the fine-structure constant, n_γ the number of photon emitted via beamstrahlung, γ the Lorentz factor, and σ_z is the bunch length. The required transversely asymmetric beams are naturally produced using damping rings (DRs) which generate a beam with asymmetric transverse normalized emittance partition ($\varepsilon_x, \varepsilon_y$). Table I summarizes typical beam parameters achieved in design

associated with few LC technologies. The latter table indicates that the required 6D phase-space brightness $\mathcal{B}_6 \equiv Q/(\varepsilon_x\varepsilon_y\varepsilon_z)$ is ~ 2 orders of magnitude smaller than those achieved in state-of-the-art radiofrequency (RF) photoinjectors [4]. Such a feature was first recognized in Ref. [5] where a linear transformation exploiting initial cross-plane correlation was proposed as a path to producing flat beams ($\varepsilon_y \ll \varepsilon_x$) using a photoinjector, i.e. without the need for a DR. In this latter work the achievable emittance ratio $\varrho \equiv \varepsilon_x/\varepsilon_y$ was comparable to the ones needed for ILC albeit at a much lower charge (0.5 nC in Ref. [5] versus the required 3.2 nC [6]).

TABLE I. Comparison of beam-parameter requirements for two conventional LC designs with parameter achieved in an RF photoinjector. The longitudinal emittance is evaluated as $\varepsilon_z \simeq \gamma\sigma_z\sigma_\delta$. The RF photoinjector used as an example is based on the L-band RF gun of the European X-ray FEL.

	ILC	CLIC	RF gun
Reference	[6]	[7]	[4]
Charge Q (nC)	3.2	0.83	2
Energy E_b (GeV)	250	380	24×10^{-3}
ε_x (μm)	10	0.9	1.3
ε_y (nm)	35	20	1.3×10^3
σ_z (mm)	0.3	0.07	2.31
σ_δ (%)	0.19	0.35	~ 0.1
ε_z (m)	0.27	0.18	$\sim 1.1 \times 10^{-4}$
\mathcal{B}_6 (pC. μm^{-3})	3.4×10^{-2}	0.25	~ 11

In this paper we further expand the technique developed in [5] by combining two cross-plane phase-space manipulations: a round-to-flat beam transformer (RFBT) [5] followed by a transverse-to-longitudinal emittance exchanger (EEX) [8, 9]. These phase-space manipulations were developed and experimentally demonstrated over the last two decades [10–14]. To illustrate

* xu@niu.edu

the potential of the technique we consider the case of the ILC parameters and show that 6D brightness ~ 2 orders of magnitude larger than the nominal ILC injector can be attained in the proposed scheme. It should be noted that a similar approach employing cross-plane phase-space manipulations was proposed in a different parameter range to mitigate the micro-bunching instability in X-ray free-electron lasers (FELs) [9]. More generally, the idea of designing photoinjectors beamlines capable of producing tunable emittance partition via emittance repartitioning and emittance exchange was extensively discussed in Refs. [15–17]. Our approach confirms that emittance partition commensurate with requirements for an LC can be attained with a simple and compact (< 50 m) beamline redistributing emittance typically produced in a conventional RF photoinjector.

II. THEORETICAL BACKGROUND

A. Transfer-matrix description of the concept

In this section we describe the underlying principle of the proposed partitioning method. We introduce the coordinate of an electron as $\mathbf{Z}^T = (x, x', y, y', z, \delta)$ where (x, x') [resp. (y, y')] represents the position-angle coordinate associated to the horizontal [resp. vertical] phase space, z is the longitudinal coordinate and δ its relative-momentum offset. All the coordinates are defined relative to a reference particle taken as the bunch barycenter. We further introduce the geometric beam emittance

$$\tilde{\varepsilon}_i \equiv [\langle \mathbf{Z}_i^2 \rangle \langle \mathbf{Z}_{i+1}^2 \rangle - \langle \mathbf{Z}_i \mathbf{Z}_{i+1} \rangle^2]^{1/2}, \quad (3)$$

for $i = 1, 3, 5$ respectively corresponding to the horizontal $\tilde{\varepsilon}_x$, vertical $\tilde{\varepsilon}_y$, and longitudinal $\tilde{\varepsilon}_z$ geometric emittances. Additionally, the normalized emittance discussed in Sec. I are $\varepsilon_\ell \equiv \gamma \tilde{\varepsilon}_\ell$ with $\ell = x, y, z$.

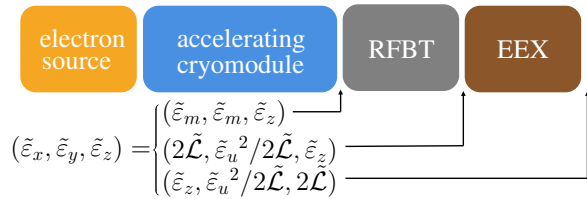


FIG. 1. Block diagram of the proposed damping-ring-free injector concept. The emittance partitions at the various stages along the injector are also listed. We defined $\tilde{\varepsilon}_m \equiv [\tilde{\varepsilon}_u^2 + \tilde{\mathcal{L}}^2]^{1/2}$. See text for details.

A high-level block diagram of the proposed approach to realizing emittance partition consistent with LC requirements appears in Fig. 1. In a first stage, the electron beam is emitted from a cathode immersed in an axial magnetic field B_c provided by a solenoidal field resulting in a “magnetized” beam downstream of the magnetic-field region. The corresponding initial beam

matrix $\Sigma \equiv \langle \mathbf{Z} \mathbf{Z}^T \rangle$ is [5, 18]

$$\Sigma_i = R_{\text{fr}} \Sigma_0 R_{\text{fr}}^T = \begin{pmatrix} A & \tilde{\mathcal{L}} J_2 & 0 \\ -\tilde{\mathcal{L}} J_2 & A & 0 \\ 0 & 0 & B \end{pmatrix}, \quad (4)$$

where $\Sigma_0 \equiv \text{diag}(\sigma_c^2, \tilde{\varepsilon}_c^2/\sigma_c^2, \sigma_c^2, \tilde{\varepsilon}_c^2/\sigma_c^2, \sigma_z^2, \tilde{\varepsilon}_z^2/\sigma_z^2)$ represent the uncorrelated beam matrix, and the matrix R_{fr} represents the fringe field experienced by the bunch as it exits the solenoidal field [5]

$$R_{\text{fr}} = \begin{pmatrix} 1 & 0 & 0 & 0 & 0 & 0 \\ 0 & 1 & -\kappa_0 & 0 & 0 & 0 \\ 0 & 0 & 1 & 0 & 0 & 0 \\ \kappa_0 & 0 & 0 & 1 & 0 & 0 \\ 0 & 0 & 0 & 0 & 1 & 0 \\ 0 & 0 & 0 & 0 & 0 & 1 \end{pmatrix}, \quad (5)$$

where $\kappa_0 \equiv \frac{eB_c}{2mc}$. In the r.h.s. of Eq. 4 the matrix $J_2 \equiv \begin{pmatrix} 0 & 1 \\ -1 & 0 \end{pmatrix}$ is skew-symmetric symplectic matrix, $\tilde{\mathcal{L}} \equiv \kappa_0 \sigma_c^2$ represents the beam magnetization (here e , m , and c are respectively the electron charge, mass, and the velocity of light) which macroscopically characterizes the beam’s average canonical angular momentum (CAM). Finally, the 2×2 matrix A is given by

$$A = \begin{pmatrix} \sigma_c^2 & 0 \\ 0 & \frac{\tilde{\varepsilon}_z^2}{\sigma_z^2} + \kappa_0^2 \sigma_c^2 \end{pmatrix}, \quad (6)$$

indicating that as the beam exits the magnetic-field region the conservation of CAM leads to a fully coupled beam with kinematical angular momentum $p_\phi = 2mc\mathcal{L}$. It should also be noted that $[\det(A)]^{1/2} = [\tilde{\varepsilon}_c^2 + \tilde{\mathcal{L}}^2]^{1/2}$ represents the projected emittance in (x, x') or (y, y') .

Downstream of the electron source the beam is injected in a linac for acceleration. The acceleration is provided by cylindrical symmetric cavity which generally support a radially axisymmetric ponderomotive focusing [19] thereby not affecting the form of the beam matrix described by Eq. 4. Downstream of the linac the beam is decoupled by applying a torque using three skew-quadrupole magnets [20] described by a total transfer matrix M . The final beam has an asymmetric transverse emittance partition [18] with corresponding beam matrix

$$\Sigma_f = M \Sigma_i M^T = \begin{pmatrix} \tilde{\varepsilon}_{x,f} T_x & 0 & 0 \\ 0 & \tilde{\varepsilon}_{y,f} T_y & 0 \\ 0 & 0 & \tilde{\varepsilon}_{z,f} T_z \end{pmatrix}, \quad (7)$$

where $T_\ell \equiv \begin{pmatrix} \beta_\ell & -\alpha_\ell \\ -\alpha_\ell & \gamma_\ell \end{pmatrix}$ with $\beta_\ell > 0$ being the betatron functions, $\alpha_\ell \equiv -\frac{1}{2} \frac{d\beta_\ell}{ds}$ measures the phase-space linear correlation and $\gamma_\ell \equiv (1 + \alpha_\ell^2)/\beta_\ell$ so that its determinant is $\det(T_\ell) = 1$. The transverse flat-beam emittances are given by [18, 21]

$$\begin{aligned} \tilde{\varepsilon}_{x,f} &\simeq 2\tilde{\mathcal{L}} \equiv \tilde{\varepsilon}_+, \text{ and} \\ \tilde{\varepsilon}_{y,f} &\simeq \frac{\tilde{\varepsilon}_u^2}{2\tilde{\mathcal{L}}} \equiv \tilde{\varepsilon}_-, \end{aligned} \quad (8)$$

where $\tilde{\varepsilon}_u \simeq [\tilde{\varepsilon}_c^2 + (\Delta\tilde{\varepsilon})^2]^{1/2}$ should be understood as the uncorrelated emittance originating from the initial photocathode intrinsic emittance $\tilde{\varepsilon}_c$ but also accounting for other emittance-degrading effects (space charge effects, geometric nonlinearities and aberrations associated with the external focusing represented by the term $\Delta\tilde{\varepsilon}$) during acceleration and transport up to the entrance of the RFBT.

A proof of principle experiment demonstrated transverse emittance ratios $\rho \simeq 100$ [10] for a charge of 0.5 nC while a recent experiment has attained an emittance ratio of $\rho \simeq 200$ for a 1-nC bunch [22].

The second stage of the proposed photoinjector consists of exchanging the horizontal and longitudinal phase spaces using a EEX beamline. The design of such beamline was extensively discussed in, e.g., Refs [8, 9, 23]. A solution for such a EEX beamline consists of a deflecting cavity flanked by two dispersive sections. In order to ensure the transfer matrix in is 2x2-block anti-diagonal in (x, x', z, δ) , the deflecting voltage V_\perp is related to the dispersion η generated by the upstream dispersive section following $1 + \kappa\eta = 1$, where $\kappa \equiv \frac{keV_\perp}{E_b}$ is the deflecting strength and $k \equiv 2\pi/\lambda$ (with λ being the deflecting-mode wavelength). Under such a condition the general transfer matrix of an EEX beamline is

$$R_{EEX} = \begin{pmatrix} 0 & 0 & F \\ 0 & E & 0 \\ F^{-1} & 0 & 0 \end{pmatrix}. \quad (9)$$

A simple implementation of an EEX beamline consists of deflecting cavity flanked by two identical dispersive section arranged as dogleg [9]. In such a case the matrix F is

$$F = \begin{pmatrix} -\frac{L}{\eta} & \eta - \frac{\xi L}{\eta} \\ -\frac{1}{\eta} & -\frac{\xi}{\eta} \end{pmatrix}, \quad (10)$$

where η and ξ are respectively the horizontal and longitudinal dispersion downstream of one dogleg and L its length. Such EEX beamlines have demonstrated near-ideal emittance exchange [11] and the formation of temporally-shaped beams [12, 24].

The final beam matrix downstream of the EEX is

$$\Sigma_e = M\Sigma M^T = \begin{pmatrix} \tilde{\varepsilon}_{z,f}T'_x & 0 & 0 \\ 0 & \tilde{\varepsilon}_{y,f}T'_y & 0 \\ 0 & 0 & \tilde{\varepsilon}_{x,f}T'_z \end{pmatrix}, \quad (11)$$

where T'_ℓ (with $\ell = x, y, z$) assumes the same form as the matrix T_ℓ introduced in Eq. 7. Consequently, the final normalized-emittance partition is

$$(\varepsilon_{x,e}, \varepsilon_{y,e}, \varepsilon_{z,e}) = (\varepsilon_{z,0}, \frac{\varepsilon_u^2}{2\mathcal{L}}, 2\mathcal{L}), \quad (12)$$

where $\mathcal{L} \equiv \gamma\tilde{\mathcal{L}}$ following our earlier convention for emittance.

B. Deviations from linear transformation

The process described in the previous Section II A idealizes the emittance partitioning and exchange by describing the associated transform with linear transfer matrices and ignoring collective effects. In this section, we briefly review some limitations of the process and corrections that were considered for the design simulated in Section III and diagrammed in Fig. 2. First, it should be noted that in our configuration we constrain the beam to have a low fractional energy spread before the RFBT which results in insignificant chromatic aberration and near-ideal transfer of eigenemittance to transverse emittance.

As far as the EEX is concerned one critical deviation from the matrix model discussed in the previous section comes from the thick-lens matrix of the deflecting cavity (labeled as T1-3 in Fig. 2) which introduces a coupling element between the horizontal and longitudinal DOF [8] and breaks the block anti-diagonal form of R_{EEX} given by Eq. 9. However, the cancellation of this term was shown to be possible using an accelerating cavity operating at zero crossing [25, 26]. Consequently, accelerating cavities were introduced (H4-5 in Fig. 2) downstream of the deflecting cavities.

The beam dynamics in the EEX section is impacted by second-order effect. In Ref. [9] it was pointed out that a proper LPS chirp could mitigate second-order aberration. In our setup given the targeted vertical emittance the introduction of the chirp would have to be done with another linac module located between the RFBT and EEX as a chirp at the entrance of the RFBT would impact the small vertical emittance due to chromatic aberration in the RFBT. Given the need to minimize the final horizontal emittance, we follow the analysis detailed in Ref. [14] to understand the source of possible final horizontal-phase-space dilution. We start by considering the phase-space coordinate of an electron downstream of the first dogleg (consisting of dipole magnets B1 and B2) we have

$$x_1 = x_0 + Lx'_0 + \eta\delta_0 + T_{122}x_0'^2 + T_{126}x_0'\delta_0 + T_{133}y_0'^2 + T_{134}y_0y_0' + T_{144}y_0'^2 + T_{166}\delta_0^2 \quad (13)$$

$$x'_1 = x'_0 + T_{233}y_0'^2 + T_{234}y_0y_0' + T_{244}y_0'^2 \quad (14)$$

for the horizontal phase space. The longitudinal phase-space coordinates are

$$z_1 = \eta x'_0 + z_0 + \xi\delta_0 + T_{522}x_0'^2 + T_{526}x_0'\delta_0 + T_{533}y_0'^2 + T_{534}y_0y_0' + T_{544}y_0'^2 + T_{566}\delta_0^2 \quad (15)$$

$$\delta_1 = \delta_0. \quad (16)$$

In the latter equations, the subscript $_0$ indicates the coordinate upstream of B1, and the T_{ijk} are the usual second-order aberration coefficients [27] associated with one dog-

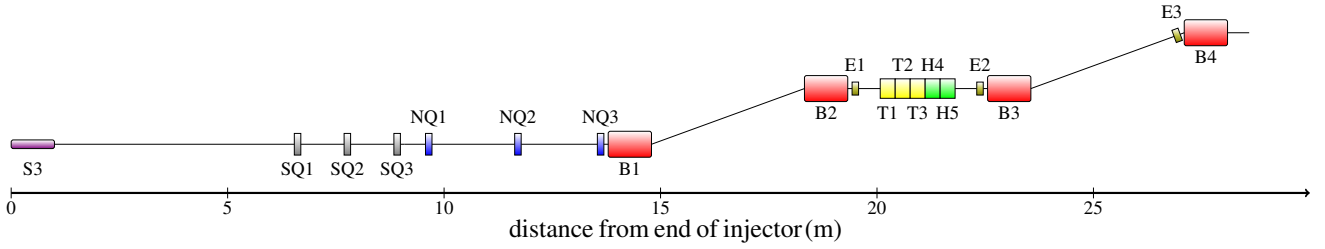


FIG. 2. Overview of the emittance manipulation beamline combining the RFBT (skew-quadropole magnets SQ1, SQ2, and SQ3) and EEX (from dipole magnet B1 to B4) insertions. The label “SQ*i*” and “NQ*i*” refer to skew- and normal-quadropole magnets, “B*i*” and “E*i*” are dipole and sextupole magnets. The elements “T*i*” and “H*i*” respectively refer to transverse-deflecting and accelerating SRF cavities; “S3” is a solenoidal magnetic lens.

leg¹.

Finally, the horizontal coordinates after the EEX section are given by

$$\begin{aligned}
 x_2 &= x_0 + T_{166}\delta_2^2 + Lx'_0 + L_d x'_0 + \delta_0\eta + Lx'_2 + L_d x'_2 \\
 &\quad + T_{122}x_0'^2 + T_{122}x_2'^2 + \eta\delta_2 + x'_0(L_a + L_c) \\
 &\quad + \kappa \left(L_a + \frac{L_c}{2} \right) (T_{522}x_0'^2 + \eta x'_0 + z_0 + \delta_0\xi) \\
 &\quad + T_{126}x_2'\delta_2 \\
 x_2' &= x'_0 + \kappa (T_{522}x_0'^2 + \eta x'_0 + z_0 + \delta_0\xi)
 \end{aligned} \tag{17}$$

where $\delta_2 \equiv \delta_0 + \kappa (x_0 + Lx'_0 + L_d x'_0 + \delta_0\eta + T_{122}x_0'^2) + \frac{L_c\kappa x'_0}{2}$, and $x_2' = x'_0 + \kappa (T_{522}x_0'^2 + \eta x'_0 + z_0 + \delta_0\xi)$ are the δ and x' coordinates after second dogleg. In latter equation we neglected geometric aberrations arising from the coupling with the (y, y') given the very low vertical emittance. Likewise, we ignore the T_{126} and T_{526} terms associated with the first dogleg since the initial $x'_0 - \delta_0$ correlation is small (ideally vanishing).

The $T_{122}x_0'^2$ and $T_{522}x_0'^2$ terms in the final horizontal coordinates can be minimized by imposing a large β_x at the entrance of EEX. The rest of the second order terms related to δ_2 and x_2' can be reduced with a initial correlation in (x_0, x'_0) and (z_0, δ_0) to produce a horizontal and longitudinal beam waist at the center of the TDC so the quantity $T_{166}\delta_2^2$, $T_{122}x_2'^2$ and $T_{126}x_2'\delta_2$ in Eq. 17 are minimized. Finally, the (x_2, x_2') coordinate downstream of B4 can be written as

$$x_2 = \eta\delta_0 - \frac{L + L_d + L_a + L_c}{2\eta}(z_0 + \xi\delta_0) \tag{19}$$

$$x_2' = \frac{-1}{\eta}(z_0 + \xi\delta_0). \tag{20}$$

The previous equation is obtained by enforcing the condition $1 + \eta\kappa = 0$ required for emittance exchange.

¹ The nonlinear aberrations arising from the deflecting cavity are ignored in this section for sake of simplicity. Their inclusions do not affect the discussion and overall aberration-correction method.

III. NUMERICAL PROOF OF CONCEPT FOR PRODUCING BEAM WITH ILC-LIKE PARAMETERS

In this section we apply the concept devised in the previous section to the case of the ILC to produce an emittance partition similar to the one produced downstream of the ILC damping ring [6]; see Table I. The design philosophy focuses on designing an injector capable of minimizing the beam emittance along all d.o.f’s upstream of the RFBT, and then optimizing the emittance repartitioning in the RFBT and emittance-exchange process in the EEX beamlines. Each of these steps is discussed below.

A. Beam generation

The conceptual design of the photoinjector beamline from the photocathode surface up to the entrance of the RFBT is diagrammed in Figure 3. The injector beamlines was modeled using the particle-in-cell beam-dynamics program IMPACT-T [28]. The electron source consists of a $1 + \frac{1}{2}$ -cell RF gun operating at $f_0 = 1.3$ GHz operating with a peak field on the cathode of $E_c = 60$ MV/m. The downstream linac consists of five TESLA-type 9-cell superconducting RF (SRF) cavities operating at a peak field of $E_L = 60$ MV/m (corresponding to an accelerating gradient $G_L \simeq E_L/2 \simeq 30$ MV/m consistent with ILC demonstrated requirement of $G_L = 31.5$ MV/m [29]). The RF gun is nested in a pair of solenoidal lenses to control the beam emittance. The beamline parameters [laser spot radius, solenoid (S1 and S2) strengths and locations, field amplitude and phase of L1] were optimized to minimize the transverse uncorrelated emittance ε_u and maximize the eigenemittance ratio $\varrho \equiv \varepsilon_+/\varepsilon_-$ at the exit of the L1. To ensure a minimal longitudinal emittance and space-charge effects, we considered a spatiotemporally shaped laser pulse with uniform three-dimensional ellipsoidal intensity distribution [30, 31].

The photoemitted electron beam mirrors the laser distribution thereby producing space-charge fields with a lin-

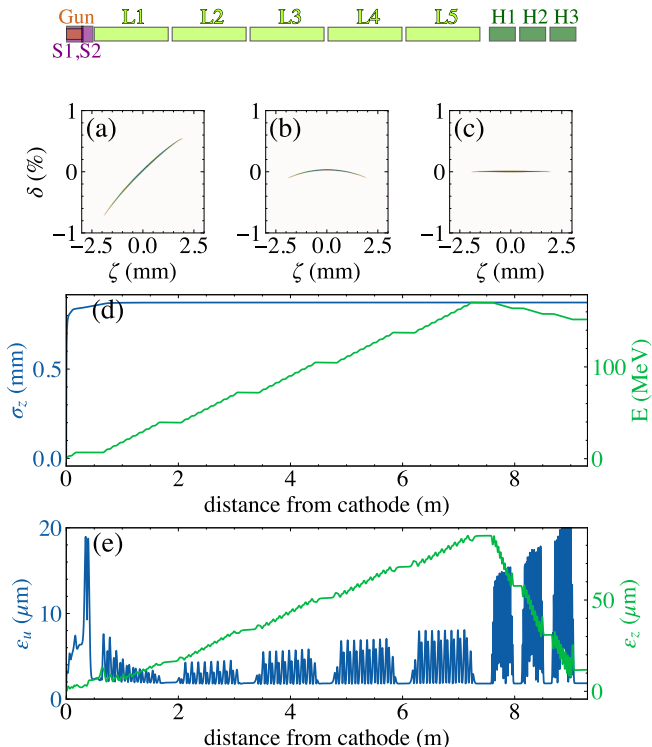


FIG. 3. Photoinjector diagram (upper schematics) and snapshots of the LPS distribution at $z = 1.88$ (a), 7.48 (b), and 9.3 m (c) from the photocathode. Evolution of the beam energy and RMS bunch length (d) and corresponding 4D transverse and longitudinal emittances (e). In the upper block diagram, S1 and S2 respectively refer to the solenoidal magnetic lenses, L1-5 are the 1.3-GHz SRF cavities, and H1-3 represent the 3.9-GHz SRF cavities. In plots (a-c) and throughout this paper, $\zeta > 0$ corresponds to the head of the bunch.

ear dependence on the spatial coordinate within the ellipsoidal bunch [32, 33]. The linear space-charge force mitigates emittance dilution and imparts a significant chirp in the longitudinal phase space (LPS). Additionally, the resulting bunch length [$\sigma_z \simeq 0.87$ mm; see Fig. 3(a)] leads the LPS to develop a quadratic correlation induced by the RF waveform; see Fig. 3(b). The linac cavities (L2-5) are operated $\varphi_L = 2^\circ$ off-crest to remove the linear LPS correlation after acceleration to 151 MeV; see Fig. 3(b). The 1.3-GHz linacs are followed by a 3rd-harmonic accelerating-cavity module operating at $f_H = 3f_0 = 3.9$ GHz to correct the quadratic correlation in the LPS and reduce the longitudinal emittance. The module comprises three SRF 3rd-harmonic cavities (H1-3) with a similar design as discussed in Ref. [34]. The cancellation of the quadratic correlation gives an 8 fold decrease in the longitudinal emittance to a final value of $\varepsilon_z \simeq 11.78$ μm ; see Fig. 3(e). The beamline parameters and resulting beam-emittance partitions are summarized in Table II.

TABLE II. Beamline settings for the proposed photoinjector and achieved normalized-emittance values at the end of the beamline. The quantities $\varepsilon_{\pm} \equiv \gamma \tilde{\varepsilon}_{\pm}$ where $\tilde{\varepsilon}_{\pm}$ is defined in Eq. 8

parameter	symbol	value	unit
charge	Q	3.2	nC
laser pulse full (and rms) duration	τ_l	10 (2.24)	ps
laser rms spot size	σ_c	1.93	mm
thermal emittance	ε_c	1.634	μm
magnetic field on cathode	B_c	226	mT
laser/gun launch phase	φ_0^a	50	deg
peak E field on cathode	E_0	60	MV/m
L2-L5 off-crest phase	φ_L	2	deg
linac peak electric field	E_L	60	MV/m
H1-H3 off-crest phase	φ_H	178.68	deg
H1-H3 peak electric field	E_H	34	MV/m
total beam energy	E_b	151	MeV
longitudinal emittance	ε_z	11.78	μm
transverse eigenemittance	ε_{-}	6.84	nm
transverse eigenemittance	ε_{+}	493.4	μm
transverse uncorrelated emittance	ε_u	1.85	μm
magnetization	\mathcal{L}	246.7	μm

^a emission phase wrt to zero-crossing.

B. Emittance Manipulation

The emittance-manipulation beamline comprising the RFBT and EEX sections was simulated using ELE-GANT [35]. The simulations account for higher-order aberrations and bunch self-interaction due to coherent synchrotron radiation (CSR). The beamline is located just after the photoinjector displayed in Fig. 3, at an energy of ~ 151 MeV. Downstream of the injector, the magnetized beam is focused by a solenoid into RFBT sections where three skew quadrupoles remove the angular momentum of the magnetized beam and transform the magnetized beam into flat beams with emittance partition downstream of the RFBT

$$(\varepsilon_{x,f}, \varepsilon_{y,f}, \varepsilon_{z,f}) = (493.40, 7.17 \times 10^{-3}, 11.82) \mu\text{m}.$$

This emittance partition confirms that the mapping of the transverse eigenemittances listed in Table II to transverse emittance is near ideal (the emittance dilution associated with the mapping $\varepsilon_{-} \rightarrow \varepsilon_y$ is 4.8%) and the longitudinal emittance is preserved (relative emittance growth of 0.3%). The flat beam is then matched into the EEX beamlines with NQ1-3 to meet the Courant-Snyder parameters requirement described in Section II B. The condition for the (z_0, δ_0) correlation is not imposed as we found the contribution of the $T_{122}x_2'^2$ term in Eq. 17 is insignificant for our beam parameters. The EEX beamline consists of two doglegs each with dipole bending angles of $(+2^\circ, -2^\circ)$, three 3.9-GHz deflecting cavities, and two 3.9-GHz accelerating cavities. The use of multiple SRF cavities is required given the demonstrated cavity

performance (maximum achievable deflecting or accelerating voltage) and our requirements. Aside from canceling the thick lens effect of TDC, the accelerating cavities are also used to partially compensate for the correlated energy spread induced by CSR. Additionally, three sextupole magnets (labeled as E1-3) are inserted in the EEX beamline to correct the nonlinearities arising from the deflecting and accelerating 3.9-GHz cavities. The voltages of the TDC and third harmonic cavities, along with the strengths of the sextupole magnet, were numerically optimized to minimize the final horizontal emittance downstream of the EEX beamline. The optimized settings for cavities and magnets appear in Table III.

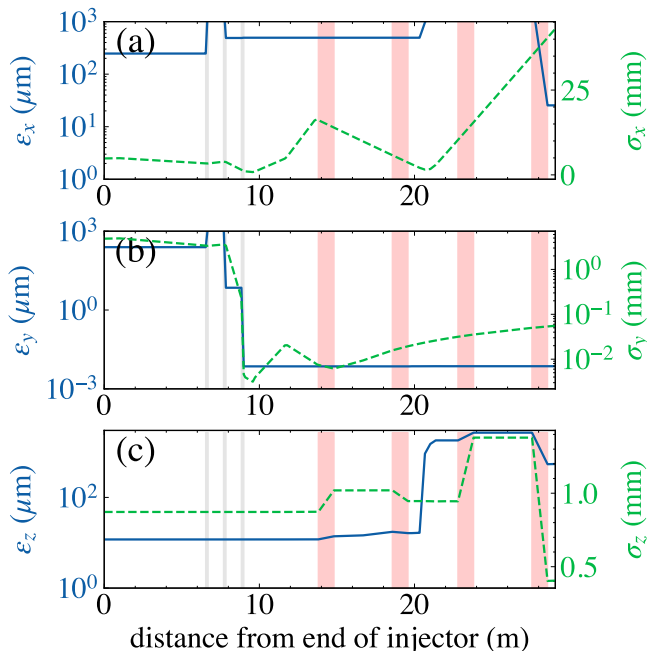


FIG. 4. Evolution of the horizontal (a), vertical (b) and longitudinal (c) emittance (blue traces) and bunch size (green dashed traces) along the emittance manipulation beamline (combining the RFBT and EEX transformations). The vertical shaded bands indicate the locations for the RFBT's skew quadrupoles (grey lines at distances < 10 m are for SQ1-3) and dipole magnets (red bands from ~ 14 m to the end of the beamline are for B1-4) associated with the EEX beamline; see Fig. 2.

The evolution of the beam emittances along the emittance-manipulation section is presented in Fig. 4 and confirms a final emittance partition of

$$(\varepsilon_{x,e}, \varepsilon_{y,e}, \varepsilon_{z,e}) = (25.47, 7.26 \times 10^{-3}, 546.34) \mu\text{m}$$

was attained corresponding to a 6D brightness $\mathcal{B}_6 \simeq 31.7 \text{ pC}/(\mu\text{m}^3)$. This 6D brightness is a factor of ~ 3 higher than the one listed under ‘‘RF gun’’ in Table I most likely due to the use of a 3D ellipsoidal photocathode-laser distribution in the present work while Ref. [4] employs a uniform-cylinder laser distribution. Snapshots of the phase-space distributions at

different stages of the beam generation and manipulation along the beamline appear in Fig. 5.

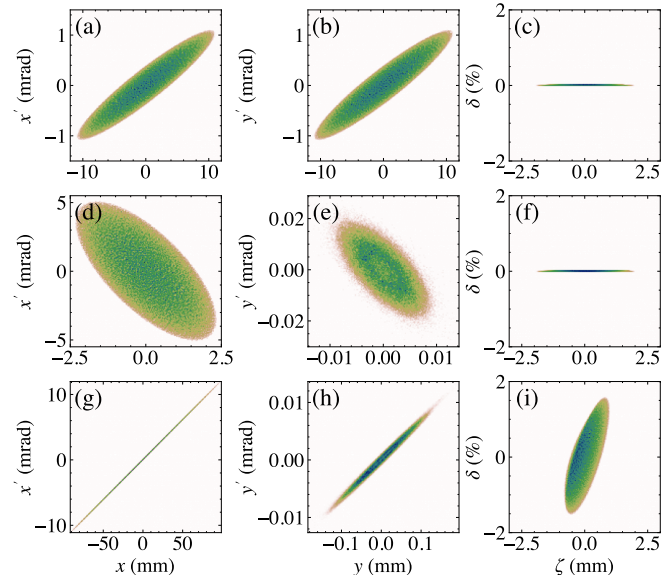


FIG. 5. Horizontal (a,d,g), vertical (b,e,h) and longitudinal (c,f,i) phase space upstream of the RFBT (a,b,c), upstream of the EEX (d,e,f) and at the exit of the EEX (g,h,i).

We evaluated the robustness of the proposed design and the sensitivity of the final transverse emittances to shot-to-shot jitters associated with amplitude and phase stability of the SRF cavities via start-to-end simulations. Specifically, we performed 1000 start-to-end simulations with different random realizations of the RF amplitude and phase for all the SRF cavities. The amplitude and phase values were randomly generated with a normal distribution with respective rms jitter of 0.01% (fractional deviation from nominal-amplitude settings) and 0.01 degree (for the 1.3 GHz cavities) and 0.03 deg (for the 3.9 GHz cavities). These tolerances are consistent with the performances of the low-level RF system at the European X-ray FEL [36]. These jitter studies confirm that the associated transverse-emittance fluctuations are acceptable – i.e. $\varepsilon_x = 25.48 \pm 0.02 \mu\text{m}$ and $\varepsilon_y = 8.13 \pm 0.98 \text{ nm}$; see corresponding histogram in Fig. 6.

C. Spin dynamics

The present requirements from high-energy physics call for 80% spin-polarized electron beams. The e^-/e^+ bunch charge ranges from fC to nC depending on the LC technology choice [37]. In most of the designs, the polarized electron beam is produced via photoemission from semiconductor Gallium-Arsenide (GaAs) photocathodes placed in a DC-gun [38]. Operation of a Gallium-Arsenide (GaAs) photocathodes in an RF gun

TABLE III. Operating parameters RFBT and EEX beamline, the magnet names refer to Fig. 2.

parameter	value	unit
skew quadrupole magnet SQ1	$k_1 = 3.71$	m^{-1}
skew quadrupole magnet SQ2	$k_1 = -7.08$	m^{-1}
skew quadrupole magnet SQ3	$k_1 = 15.76$	m^{-1}
sextupole magnet E1	$k_2 = -15.67$	m^{-2}
sextupole magnet E2	$k_2 = -1.08$	m^{-2}
sextupole magnet E3	$k_2 = -0.03$	m^{-2}
doglegs dispersion η	-1.67	m
TDC section kick strength κ	6	m^{-1}
dipole magnet B1-B4 angles	2	deg
T1 deflecting voltage	3.72	MV
T2 deflecting voltage	3.72	MV
T3 deflecting voltage	3.66	MV
H4 accelerating voltage	5.81	MV
H5 accelerating voltage	5.91	MV

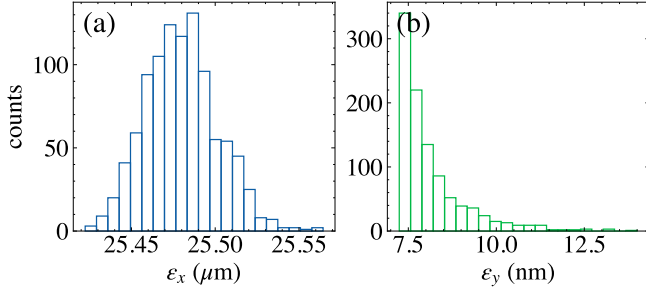


FIG. 6. Histogram of final horizontal (a) and vertical (b) emittances simulated downstream of the EEX beamline for 1000 realizations of SRF-cavity random phase and amplitude jitters.

remains a challenge and has been the subject of intense research [39–41]. The photoinjector is expected to produce a longitudinally spin-polarized electron beam with most of the electrons' spin vector $\mathbf{S} = S_z \hat{z}$.

The evolution of the spin in an externally-applied magnetic field \mathbf{B} can be described by the classical spin vector \mathbf{S} under the action of a semiclassical spin precession vector $\boldsymbol{\Omega}$ via the BMT equation [42]

$$\frac{d\mathbf{S}}{dt} = \mathbf{S} \times \boldsymbol{\Omega} \quad (21)$$

with,

$$\boldsymbol{\Omega} = \frac{e}{m} \left[\left(a + \frac{1}{\gamma} \right) \mathbf{B} - \frac{a\gamma}{\gamma+1} (\boldsymbol{\beta} \cdot \mathbf{B}) \boldsymbol{\beta} - \left(a + \frac{1}{\gamma+1} \right) \boldsymbol{\beta} \times \frac{\mathbf{E}}{c} \right], \quad (22)$$

where a is anomalous magnetic moment and $\boldsymbol{\beta} \equiv \frac{\mathbf{v}}{c}$ with \mathbf{v} being the velocity.

The spin dynamics of the particle distribution was investigated with the beam-dynamics program BMAD [43]

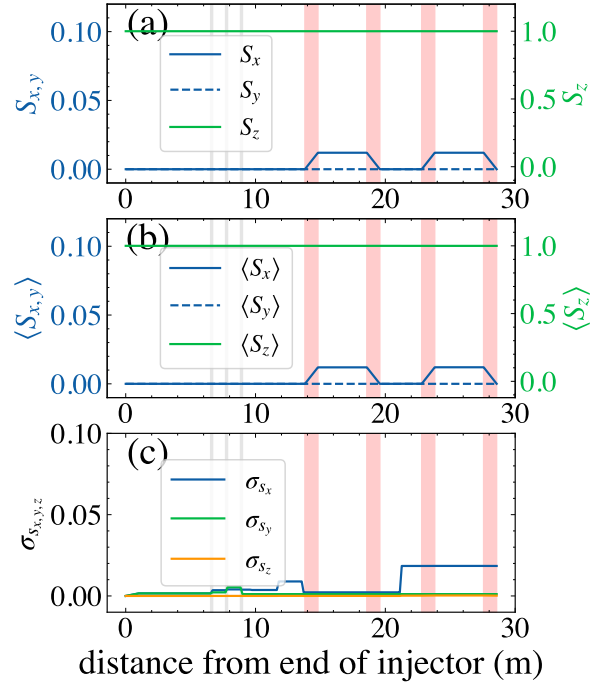


FIG. 7. Evolution of the spin components along the emittance-manipulation beamline. Spin components associated with the reference particle $\mathbf{S}^T = (S_x, S_y, S_z)$ (a), statistical average $\langle \mathbf{S} \rangle$ (b) and RMS value $\langle \mathbf{S}^2 \rangle^{1/2}$ (c) computed over the macroparticle distribution. The vertical shaded bands indicate the locations for the RFBT's skew quadrupoles (grey lines at distances < 10 m are for SQ1-3) and dipole magnets (red bands from ~ 14 m to the end of the beamline are for B1-4) associated with the EEX beamline; see Fig. 2.

which implements a Romberg integration of the spin rotation matrix. Figure 7 presents the evolution of spin-vector components through the RFBT and EEX sections shown in Fig. 2. The initial conditions are such that the beam is 100% longitudinally spin-polarized $\mathbf{S}^T = (0, 0, 1)$. The simulation indicate that the RFBT does not impact the spin (no depolarization is observed) while the EEX beamline yield a small depolarization with final mean and RMS longitudinal spin values being respectively $\langle \mathbf{S}_e \rangle^T = (5.41 \times 10^{-5}, -1.39 \times 10^{-8}, 0.99)$ and $(\sigma_{S_{x,e}}, \sigma_{S_{y,e}}, \sigma_{S_{z,e}}) = (1.84 \times 10^{-2}, 1.12 \times 10^{-3}, 1.81 \times 10^{-4})$. confirming that the longitudinal depolarization $\frac{\sigma_{S_{z,e}}}{\langle S_{z,e} \rangle} \sim \mathcal{O}(10^{-4})$ is insignificant.

D. Enhanced Luminosity

The noted reduction in longitudinal emittance combined with longitudinal bunch compression could further enhance the luminosity given the scaling $\mathfrak{L} \propto \sigma_z^{-1/2}$; see Eq. 2. In addition to improving luminosity, colliding short bunches also mitigate beamstrahlung-radiation losses thereby allowing the particles to experience ex-

extreme electromagnetic fields to probe non-perturbative quantum-electrodynamics effects [44]. The photoinjector described in Sec. III A produces a final LPS with bunch length $\sigma_{z,e} = 407 \mu\text{m}$; see Fig. 8(a). Further accelerating the beam to 5 GeV [see Fig. 8(b)] and considering a single-stage bunch compressor (as implemented in the nominal ILC design downstream of the DR [45]) can reduce the bunch length to $\sigma'_z \simeq 23 \mu\text{m}$; see Fig. 8(c,d). The simulations presented in Fig. 8 were performed with

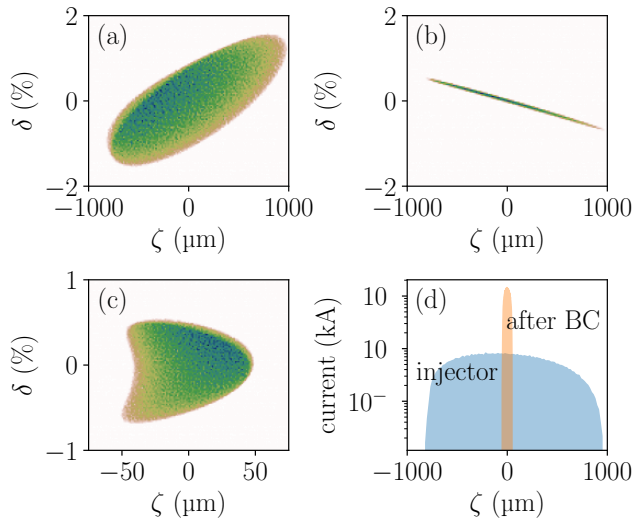


FIG. 8. Snapshots of the LPS distributions at the exit of the photoinjector (a), after acceleration to 5 GeV (b) and downstream of a single-stage bunch compressor (c) and current distribution (d) at the injector exit (“injector”) and downstream of the bunch compressor (“after BC”).

a 1D single-particle model of the longitudinal beam dynamics. In the model, the linac accelerates the beam from 151 MeV to 5 GeV. The linac runs 15° off-crest to impart the required correlated energy spread for maximum compression in a downstream bunch compressor. The bunch compressor is modeled by its longitudinal dispersion $R_{56} = 14.9 \text{ cm}$ (in our convention $R_{56} > 0$ corresponds to a chicane-like compressor).

IV. CONCLUSION

In summary, we demonstrated a beamline composed of two cascaded cross-plane manipulations that could produce an electron beam with a final transverse-emittance partition comparable to the one attained downstream of the damping ring in the proposed ILC design. Ad-

ditionally, our method produces electron bunches with brightness ~ 2 orders of magnitude higher than the ILC design. The enhanced brightness could further increase the luminosity by producing shorter bunches at the interaction point. Finally, the proposed scheme presents a substantial cost and complexity reduction compared to a damping ring. Although our focus was on demonstrating the application of the scheme to ILC-like parameters, the concept also be optimized for other LC designs.

Yet, the integration of the proposed technique in future LC designs is contingent on the successful generation of spin-polarized beams from RF guns. Likewise, the method could also apply to positron beams pending the availability of low-emittance positron sources such as, e.g., recently proposed based on an electrostatic trap [46], or relying on bremsstrahlung by impinging electron beams on thin targets [47].

Ultimately, the emittance-manipulation method discussed in this paper will require a vigorous R&D program on sources of bright spin-polarized electron and positron beams to be deployed in a future LC design. Two complementary experiments aimed at testing the proposed concepts are currently in preparation at the Argonne Wakefield Accelerator (AWA) [22] and the Superconducting Test Facility (STF) at the High Energy Accelerator Research Organization (KEK) [48].

V. ACKNOWLEDGEMENTS

We thank Dr. Eliana Gianfelice-Wendt (FNAL) for her suggestions regarding spin-dynamics simulations along with Drs. Chris Mayes (SLAC) and David Sagan (Cornell University) for their help with the spin-tracking feature of BMAD. We appreciate discussions with Dr. Zachary Liptak (Hiroshima University). PP is grateful to Dr. Spencer Gessner (SLAC) for sharing a draft manuscript [46] on bright positron sources. This research was initiated in the framework of the “US-DOE-Japan cooperation in High-Energy Physics” program. This work was supported by the U.S. Department of Energy (DOE), Office of Science, under award No. DE-SC0018656 with Northern Illinois University (NIU) and contract No. DE-AC02-06CH11357 with Argonne National Laboratory (ANL).

The computing resources used for this research were provided on BEBOP, a high-performance computing cluster operated by the Laboratory Computing Resource Center (LCRC) at ANL.

-
- [1] J. Ellis and I. Wilson, New physics with the compact linear collider, *Nature* **409**, 431 (2001).
 [2] G. Dugan, Advanced accelerator system requirements for

- future linear colliders, *AIP Conference Proceedings* **737**, 29 (2004).
 [3] K. Yokoya, Beam-beam interaction in linear collider, *AIP*

- Conference Proceedings **592**, 185 (2001).
- [4] M. Krasilnikov, F. Stephan, G. Asova, H.-J. Grabosch, M. Groß, L. Hakobyan, I. Isaev, Y. Ivanisenko, L. Jachmann, M. Khojoyan, G. Klemz, W. Köhler, M. Mahgoub, D. Malyutin, M. Nozdrin, A. Oppelt, M. Otevrel, B. Petrosyan, S. Rimjaem, A. Shapovalov, G. Vashchenko, S. Weidinger, R. Wendorff, K. Flöttmann, M. Hoffmann, S. Lederer, H. Schlarb, S. Schreiber, I. Templin, I. Will, V. Paramonov, and D. Richter, Experimentally minimized beam emittance from an l -band photoinjector, *Phys. Rev. ST Accel. Beams* **15**, 100701 (2012).
 - [5] R. Brinkmann, Y. Derbenev, and K. Flöttmann, A low emittance, flat-beam electron source for linear colliders, *Phys. Rev. ST Accel. Beams* **4**, 053501 (2001).
 - [6] N. Phinney, N. Toge, and N. Walker, *ILC reference design report volume 3 - accelerator* (2007).
 - [7] T. CLIC, T. Charles, P. Giansiracusa, T. Lucas, R. Rasool, M. Volpi, C. Balazs, K. Afanaciev, V. Makarenko, A. Patapenka, *et al.*, The compact linear collider (cllc)-2018 summary report, *arXiv preprint arXiv:1812.06018* (2018).
 - [8] M. Cornacchia and P. Emma, Transverse to longitudinal emittance exchange, *Phys. Rev. ST Accel. Beams* **5**, 084001 (2002).
 - [9] P. Emma, Z. Huang, K.-J. Kim, and P. Piot, Transverse-to-longitudinal emittance exchange to improve performance of high-gain free-electron lasers, *Phys. Rev. ST Accel. Beams* **9**, 100702 (2006).
 - [10] P. Piot, Y.-E. Sun, and K.-J. Kim, Photoinjector generation of a flat electron beam with transverse emittance ratio of 100, *Phys. Rev. ST Accel. Beams* **9**, 031001 (2006).
 - [11] J. Ruan, A. S. Johnson, A. H. Lumpkin, R. Thurman-Keup, H. Edwards, R. P. Fliiller, T. W. Koeth, and Y.-E. Sun, First observation of the exchange of transverse and longitudinal emittances, *Phys. Rev. Lett.* **106**, 244801 (2011).
 - [12] Y.-E. Sun, P. Piot, A. Johnson, A. H. Lumpkin, T. J. Maxwell, J. Ruan, and R. Thurman-Keup, Tunable subpicosecond electron-bunch-train generation using a transverse-to-longitudinal phase-space exchange technique, *Phys. Rev. Lett.* **105**, 234801 (2010).
 - [13] L. Groening, M. Maier, C. Xiao, L. Dahl, P. Gerhard, O. K. Kester, S. Mickat, H. Vormann, M. Vossberg, and M. Chung, Experimental proof of adjustable single-knob ion beam emittance partitioning, *Phys. Rev. Lett.* **113**, 264802 (2014).
 - [14] G. Ha, M. Cho, W. Gai, K.-J. Kim, W. Namkung, and J. Power, Perturbation-minimized triangular bunch for high-transformer ratio using a double dogleg emittance exchange beam line, *Phys. Rev. Accel. Beams* **19**, 121301 (2016).
 - [15] N. Yampolsky, B. Carlsten, R. Ryne, K. Bishofberger, S. Russell, and A. Dragt, *Controlling electron-beam emittance partitioning for future x-ray light sources* (2010), [arXiv:1010.1558 \[physics.acc-ph\]](https://arxiv.org/abs/1010.1558).
 - [16] B. E. Carlsten, K. A. Bishofberger, L. D. Duffy, S. J. Russell, R. D. Ryne, N. A. Yampolsky, and A. J. Dragt, Arbitrary emittance partitioning between any two dimensions for electron beams, *Phys. Rev. ST Accel. Beams* **14**, 050706 (2011).
 - [17] L. D. Duffy and A. J. Dragt, Chapter one - utilizing the eigen-emittance concept for bright electron beams, in *Advances in Imaging and Electron Physics*, Vol. 193, edited by P. W. Hawkes (Elsevier, 2016) pp. 1–44.
 - [18] K.-J. Kim, Round-to-flat transformation of angular-momentum-dominated beams, *Phys. Rev. ST Accel. Beams* **6**, 104002 (2003).
 - [19] J. Rosenzweig and L. Serafini, Transverse particle motion in radio-frequency linear accelerators, *Phys. Rev. E* **49**, 1599 (1994).
 - [20] Y. Sun, P. Piot, K.-J. Kim, N. Barov, S. Lidia, J. Santucci, R. Tikhoplav, and J. Wennerberg, Generation of angular-momentum-dominated electron beams from a photoinjector, *Phys. Rev. ST Accel. Beams* **7**, 123501 (2004).
 - [21] A. Burov, S. Nagaitsev, and Y. Derbenev, Circular modes, beam adapters, and their applications in beam optics, *Phys. Rev. E* **66**, 016503 (2002).
 - [22] T. Xu, D. S. Doran, W. Liu, P. Piot, J. G. Power, C. Whiteford, and E. Wisniewski, Demonstration of eigen-to-projected emittance mapping for an ellipsoidal electron bunch, *Phys. Rev. Accel. Beams* **25**, 044001 (2022).
 - [23] E. A. Nanni and W. S. Graves, Aberration corrected emittance exchange, *Phys. Rev. ST Accel. Beams* **18**, 084401 (2015).
 - [24] G. Ha, M. H. Cho, W. Namkung, J. G. Power, D. S. Doran, E. E. Wisniewski, M. Conde, W. Gai, W. Liu, C. Whiteford, Q. Gao, K.-J. Kim, A. Zholents, Y.-E. Sun, C. Jing, and P. Piot, Precision control of the electron longitudinal bunch shape using an emittance-exchange beam line, *Phys. Rev. Lett.* **118**, 104801 (2017).
 - [25] A. A. Zholents and M. S. Zolotarev, *A new type of bunch compressor and seeding of short wave length coherent radiation*, Tech. Rep. ANL/APS/LS-327 (Argonne National Laboratory, 2011).
 - [26] D. Xiang and A. Chao, Emittance and phase space exchange for advanced beam manipulation and diagnostics, *Phys. Rev. ST Accel. Beams* **14**, 114001 (2011).
 - [27] K. L. Brown, A First- and Second-Order Matrix Theory for the Design of Beam Transport Systems and Charged Particle Spectrometers, in *Advances in Particle Physics, Volume I*, edited by R. L. Cool and R. E. Marshak (1968) p. 71, also available as SLAC technical report SLAC-R-075, SLAC-75.
 - [28] J. Qiang, S. Lidia, R. D. Ryne, and C. Limborg-Deprey, Three-dimensional quasistatic model for high brightness beam dynamics simulation, *Phys. Rev. ST Accel. Beams* **9**, 044204 (2006).
 - [29] D. Broemmelsiek, B. Chase, D. Edstrom, E. Harms, J. Leibfritz, S. Nagaitsev, Y. Pischalnikov, A. Romanov, J. Ruan, W. Schappert, V. Shiltsev, R. Thurman-Keup, and A. Valishev, Record high-gradient SRF beam acceleration at fermilab, *New Journal of Physics* **20**, 113018 (2018).
 - [30] Y. Li and J. W. Lewellen, Generating a quasiellipsoidal electron beam by 3D laser-pulse shaping, *Phys. Rev. Lett.* **100**, 074801 (2008).
 - [31] Y. Li, S. Chemerisov, and J. Lewellen, Laser pulse shaping for generating uniform three-dimensional ellipsoidal electron beams, *Phys. Rev. ST Accel. Beams* **12**, 020702 (2009).
 - [32] P. M. Lapostolle, *Effets de la charge d'espace dans un accélérateur linéaire à protons*, Tech. Rep. CERN-AR-Int-SG-65-15 (CERN, Geneva, 1965).
 - [33] O. J. Luiten, S. B. van der Geer, M. J. de Loos, F. B. Kiewiet, and M. J. van der Wiel, How to realize uniform three-dimensional ellipsoidal electron bunches,

- Phys. Rev. Lett.* **93**, 094802 (2004).
- [34] M. Bertucci, A. Bignami, A. Bosotti, P. Michelato, L. Monaco, C. Pagani, R. Paparella, D. Sertore, C. Miano, P. Pierini, and J. Chen, Performance analysis of the European X-ray Free Electron Laser 3.9 GHz superconducting cavities, *Phys. Rev. Accel. Beams* **22**, 082002 (2019).
- [35] M. Borland, ELEGANT: A Flexible SDDS-Compliant Code for Accelerator Simulation, in *6th International Computational Accelerator Physics Conference (ICAP 2000)* (2000).
- [36] M. Omet *et al.*, LLRF Operation and Performance at the European XFEL, in *Proc. 9th International Particle Accelerator Conference (IPAC'18), Vancouver, BC, Canada, April 29-May 4, 2018*, International Particle Accelerator Conference No. 9 (JACoW Publishing, Geneva, Switzerland, 2018) pp. 1934–1936, <https://doi.org/10.18429/JACoW-IPAC2018-WEPAF051>.
- [37] ALEGRO Collaboration, *Towards an advanced linear international collider* (2019).
- [38] C. K. Sinclair, P. A. Adderley, B. M. Dunham, J. C. Hansknecht, P. Hartmann, M. Poelker, J. S. Price, P. M. Rutt, W. J. Schneider, and M. Steigerwald, Development of a high average current polarized electron source with long cathode operational lifetime, *Phys. Rev. ST Accel. Beams* **10**, 023501 (2007).
- [39] K. Aulenbacher, G. Suberlucq, H. Tang, J. Sheppard, G. A. Mulhollan, J. P. Delahaye, J. Madsen, J. E. Clendenin, R. Bossart, and H. Braun, *RF guns and the production of polarized electrons*, Tech. Rep. (CERN, Geneva, 1996).
- [40] A. V. Aleksandrov, E. S. Konstantinov, P. V. Logatchev, A. A. Starostenko, and A. V. Novokhatskii, High Power Test of GaAs Photocathode in RF Gun, in *6th European Particle Accelerator Conference, Stockholm, Sweden (EPAC98)* (1998) pp. 1450–1452.
- [41] R. Fliller, T. Anderson, H. Edwards, H. Bluem, T. Schultheiss, C. Sinclair, and M. Huening, Progress on using NEA cathodes in an rf gun, in *Proceedings of the 2005 Particle Accelerator Conference* (2005) pp. 2708–2710.
- [42] V. Bargmann, L. Michel, and V. L. Telegdi, Precession of the polarization of particles moving in a homogeneous electromagnetic field, *Phys. Rev. Lett.* **2**, 435 (1959).
- [43] D. Sagan, BMAD: A relativistic charged particle simulation library, *Computational accelerator physics. Proceedings, 8th International Conference, ICAP 2004, St. Petersburg, Russia, June 29-July 2, 2004*, *Nucl. Instrum. Meth.* **A558**, 356 (2006), proceedings of the 8th International Computational Accelerator Physics Conference.
- [44] V. Yakimenko, S. Meuren, F. Del Gaudio, C. Baumann, A. Fedotov, F. Fiuza, T. Grismayer, M. J. Hogan, A. Pukhov, L. O. Silva, and G. White, Prospect of studying nonperturbative QED with beam-beam collisions, *Phys. Rev. Lett.* **122**, 190404 (2019).
- [45] A. Latina and N. Solyak, Single-Stage Bunch Compressor for ILC-SB2009, *Conf. Proc. C* **100523**, THPE042 (2010).
- [46] R. Hessami and S. Gessner, *A Compact Source of Positron Beams with Small Thermal Emittance*, Tech. Rep. (SLAC, Menlo Park, CA, 2022) to be published (private communication with S. Gessner).
- [47] D. Abbott, P. Adderley, A. Adeyemi, P. Aguilera, M. Ali, H. Areti, M. Baylac, J. Benesch, G. Bosson, B. Cade, A. Camsonne, L. S. Cardman, J. Clark, P. Cole, S. Covert, C. Cuevas, O. Dadoun, D. Dale, H. Dong, J. Dumas, E. Fanchini, T. Forest, E. Forman, A. Freyberger, E. Froidefond, S. Golge, J. Grames, P. Guèye, J. Hansknecht, P. Harrell, J. Hoskins, C. Hyde, B. Josey, R. Kazimi, Y. Kim, D. Machie, K. Mahoney, R. Mammei, M. Marton, J. McCarter, M. McCaughan, M. McHugh, D. McNulty, K. E. Mesick, T. Michaelides, R. Michaels, B. Moffit, D. Moser, C. Muñoz Camacho, J.-F. Muraz, A. Opper, M. Poelker, J.-S. Réal, L. Richardson, S. Setiniyaz, M. Stutzman, R. Suleiman, C. Tennant, C. Tsai, D. Turner, M. Ungaro, A. Variola, E. Voutier, Y. Wang, and Y. Zhang (PEPPo Collaboration), Production of highly polarized positrons using polarized electrons at mev energies, *Phys. Rev. Lett.* **116**, 214801 (2016).
- [48] M. Kuriki *et al.*, High Aspect Ratio Beam Generation with the Phase-space Rotation Technique for Linear Colliders, in *29th International Linear Accelerator Conference* (2018) p. THPO005.